# Supplementary Figures

Supplementary Figure 1: The eastern Mediterranean Sea. Colours indicate subbasins of the eastern Mediterranean Sea (EMS) with names given in the plot. Contour lines indicate the early Holocene bathymetry. Boxes indicate averaging areas used in other figures.
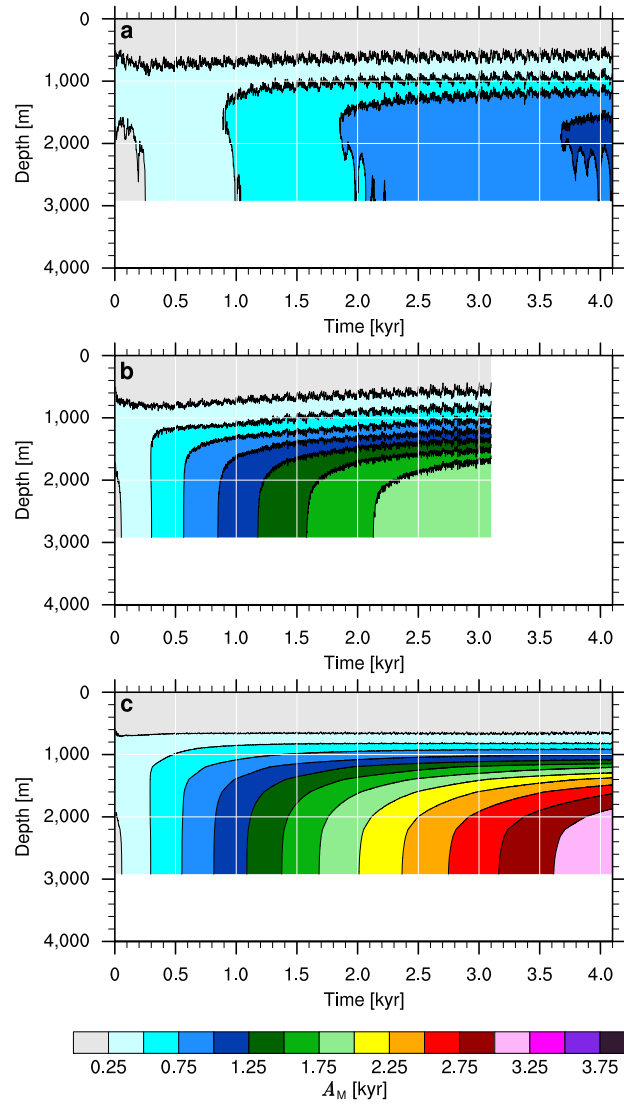
**Supplementary Figure 2: Modelled apparent water age averaged over the Levantine Sea.** Hovmöller diagram of the apparent water age (A_{M}) for the Baseline experiment (same for 3xNutri experiment) (**a**), Nile experiment (**b**), and IniGlac experiment (same for IniGlac+3xNutri) (**c**). Averaging area as indicated by the box in the Levantine Sea in Supplementary Figure 1.
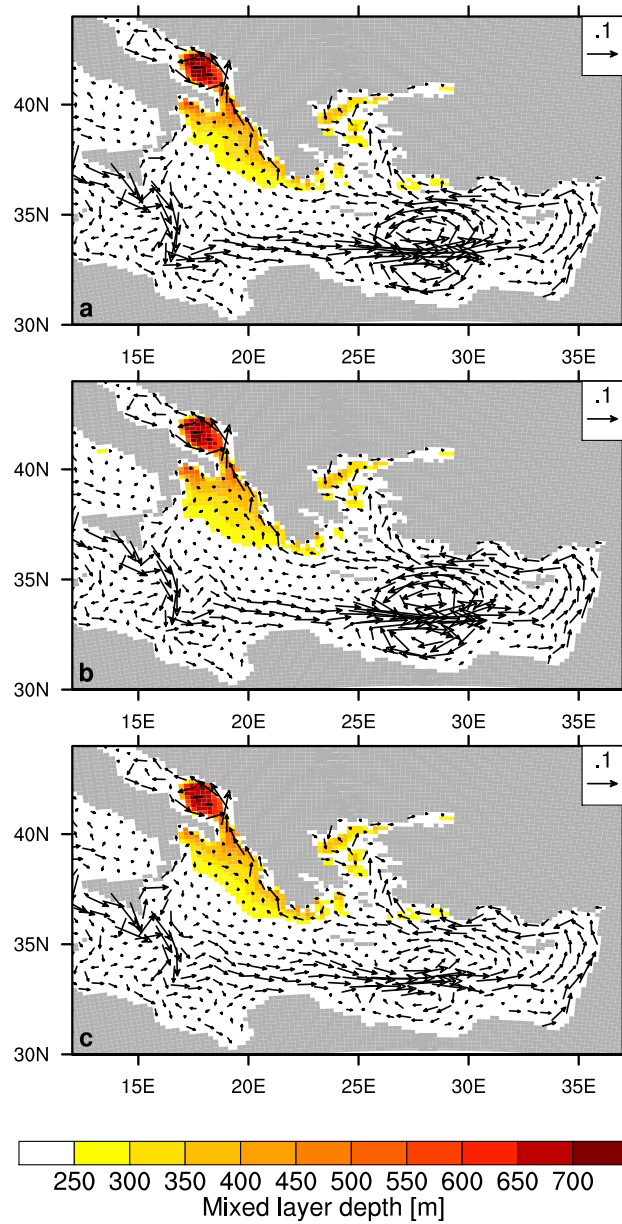
Supplementary Figure 3: Near surface circulation and mixed layer depth in March. Circulation in the Baseline experiment (same for 3xNutri experiment) (**a**), Nile experiment (**b**), and IniGlac experiment (same for IniGlac+3xNutri experiment) (**c**). Vectors represent both the direction and speed [m s^{-1}] of the annual mean circulation at 25 m depth. Mixed layer depth diagnosed in the model at the depth where the potential density is 0.125 kg m^{-3} larger than at the surface. Results are averaged between the simulation years 3,001 and 3,100.
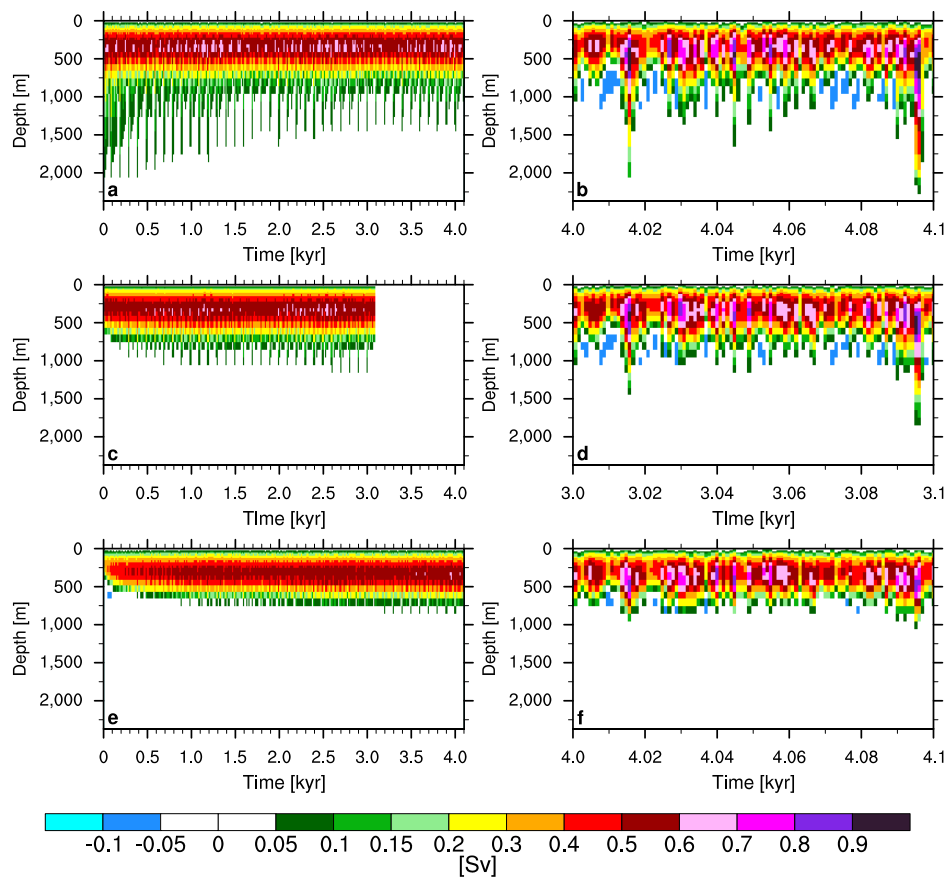
Supplementary Figure 4: Annual mean water transport rate. Hovmöller diagrams of the transport profile at 38.82°N between Italy and Greece for the entire simulation period smoothed with a 20-year running average (left column), and unsmoothed annual mean values for the last 100 years of simulation (right column) for the Baseline experiment (same for 3xNutri experiment) (**a,b**), Nile experiment (**c,d**) and IniGlac experiment (same for IniGlac+3xNutri experiment) (**e,f**). The maximum depth of the transect is given by the maximum depth at 2,370 m in this location.

4
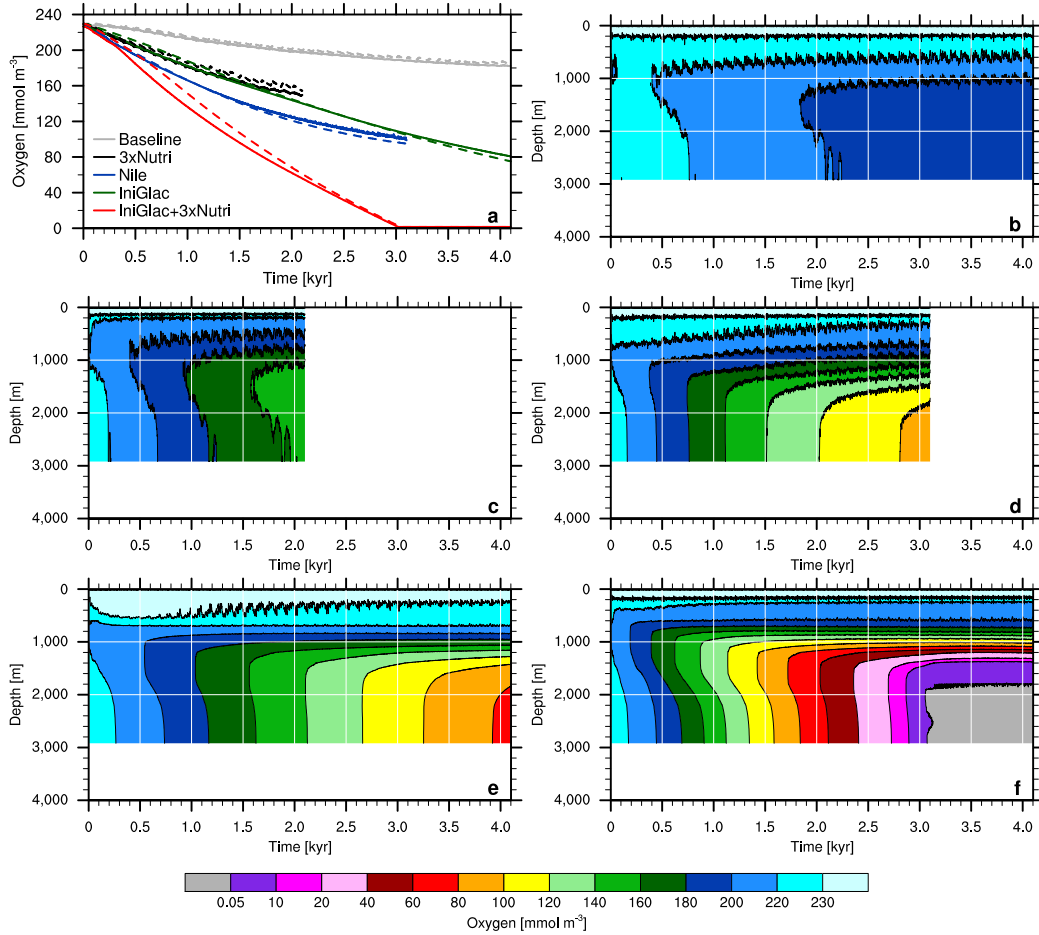
Supplementary Figure 5: Annual mean oxygen concentration averaged over the Levantine Sea. Time series of the oxygen concentration in 1,800 m (solid line) and 2,920 m (dashed line) (**a**). Hovmöller diagrams of the oxygen concentration for the Baseline experiment (**b**), 3xNutri experiment (**c**), Nile experiment (**d**), IniGlac experiment (**e**), and IniGlac+3xNutri experiment (**f**). Note the nonlinear colour scale. Extent of the Levantine Sea averaging area is given in Supplementary Figure 1.

5
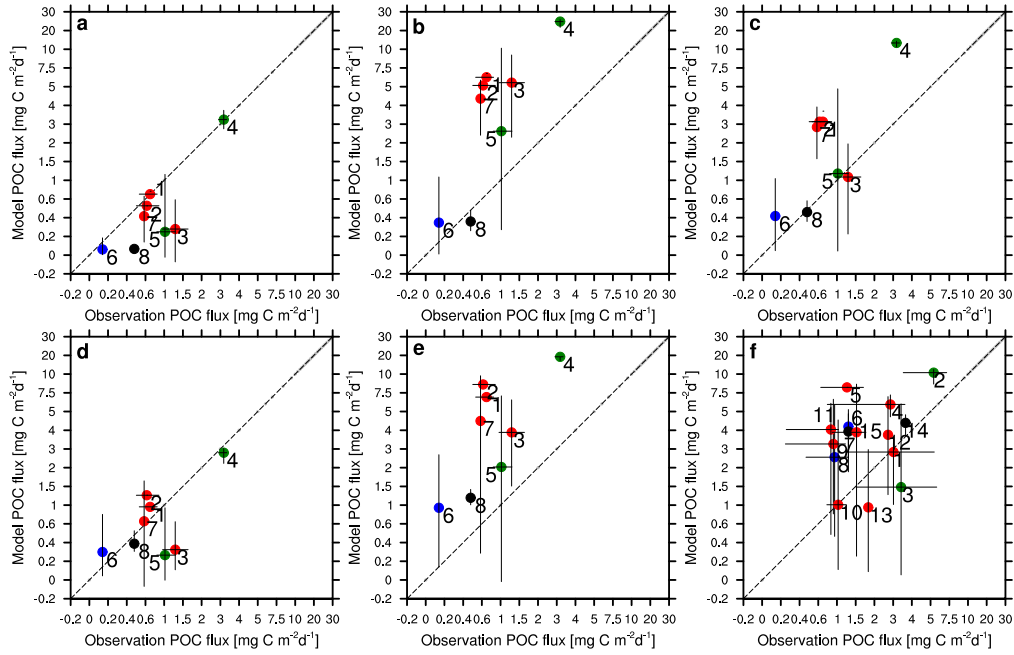
Supplementary Figure 6: Sediment particulate organic carbon burial flux versus modelled burial flux. 100-year mean values of the particulate organic carbon (POC) burial flux of the Baseline experiment (years 4,001-4,100) (**a**), 3xNutri experiment (years 2,001-2,100) (**b**), Nile experiment (years 3,001-3,100) (**c**), IniGlac experiment (years 4,001-4,100) (**d**), IniGlac+3xNutri experiment (years 2,801-2,900) (**e**), IniGlac+3xNutri experiment (years 4,001-4,100) (**f**). Points represent the averaged observed flux of the sediment cores versus modelled fluxes averaged in a 3x3 gridbox window around the core location for those grid boxes with a model depth within ±200 m of the model depth at the core location. Black horizontal lines represent the maximum temporal variation of the observations for the pre-sapropel period (10.5-11.5 kyr ago) (**a-e**), and the sapropel period (6.5-9.5 kyr ago) (**f**), unless not otherwise given in the corresponding sediment core data source (see Supplementary Note 2 for more details). The black vertical lines show the maximum small-scale spatial variation of the modelled values within the 3x3 gridbox window and within ±200 m of the model depth at the core location. Colours indicate the water depth of the model gridbox at the core locations: green < 1,000 m, 1,000 m ≤ red < 2,000 m, 2,000 m ≤ blue < 3,000 m, black ≥ 3,000 m. Geographic position of sediment core labels is given in the main text (main text Fig. 4). Note the nonlinear axes scales. Sediment core data, sorted after label number, for the pre-sapropel time slice were derived from sites: Geo-Tü SL114[1]; Geo-Tü SL119[2]; Geo-Tü SL148, Geo-Tü SL112, Geo-Tü SL123[3]; M40/4_SL71[4,5]; MD84-641[6]; ODP site 160-964A[7]. Sediment core data, sorted after label number, for the sapropel time slice were derived from sites: Geo-Tü SL148, Geo-Tü SL112, Geo-Tü SL123[3]; Geo-Tü SL114[1]; Geo-Tü SL119[2]; BC19, SL114[8]; M40/4_SL71, M51/3_569, M51/3_563, M51/3_562[4,5]; SL60, MD90-917[9]; ODP site 160-964A[7]; MD84-641[6].
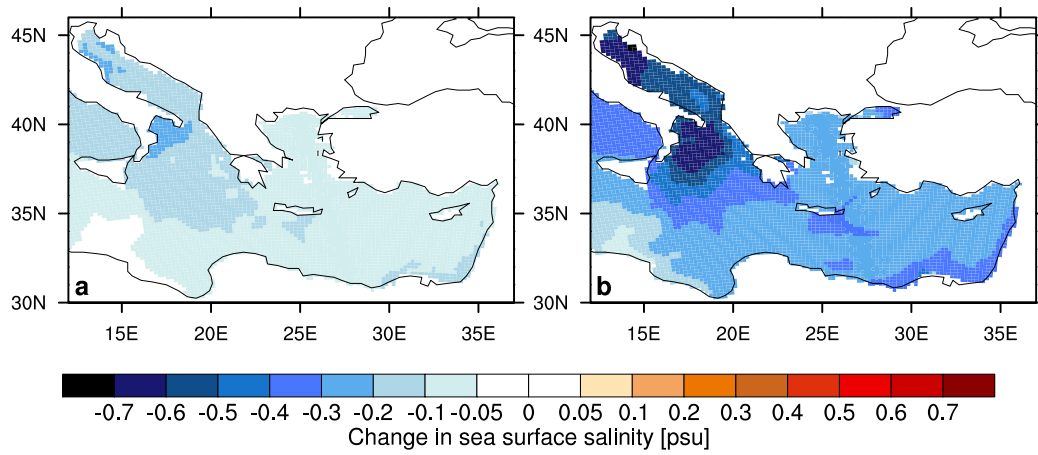
Supplementary Figure 7: Maps of the change in sea surface salinity. Change in the sea surface salinity of the IniGlac_-2 experiment (**a**) and the IniGlac_-6 experiment (**b**), each relative to the IniGlac experiment. Annual average between the simulation years 4,001-4,100 (**a**) and years 4,201-4,300 (**b**). See Supplementary Note 3 for more details on these experiments.
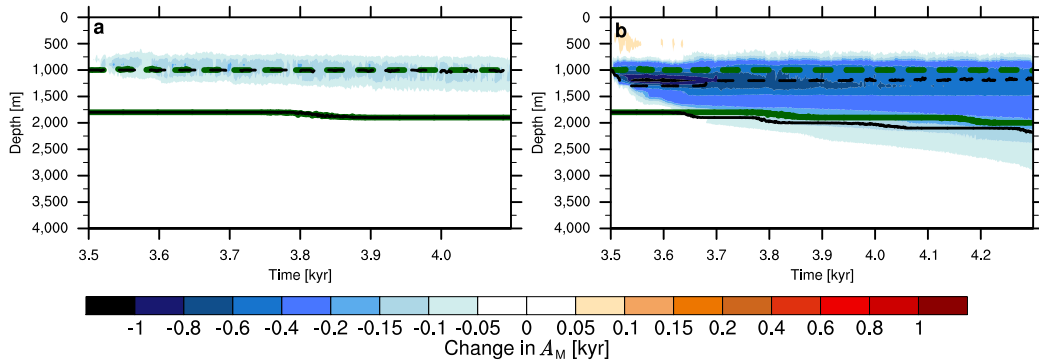
Supplementary Figure 8: Hovmöller diagrams of the change in A_{M}, the ventilation-stagnation interface, and the depth interface between the well-ventilated upper ocean and the partially ventilated ocean. Change of the A_{M} relative to the IniGlac experiment for the IniGlac_-2 experiment (**a**) and the IniGlac_-6 experiment (**b**), each averaged over the Ionian Sea. The dashed lines mark the depth interface between the well-ventilated upper ocean and the partially ventilated ocean (WPI), the solid lines mark the depth of the ventilation-stagnation interface (VSI) (see Supplementary Note 3 for definitions). The green lines show results of the VSI and WPI of the IniGlac experiment (**a**,**b**), the black lines for the IniGlac_-2 experiment (**a**) and the IniGlac_-6 experiment (**b**). Note the different x-axis scales and that the green lines are invisible when they are perfectly overlain by the black lines. The Ionian Sea averaging area is given in Supplementary Figure 1. See Supplementary Note 3 for more details on these experiments.
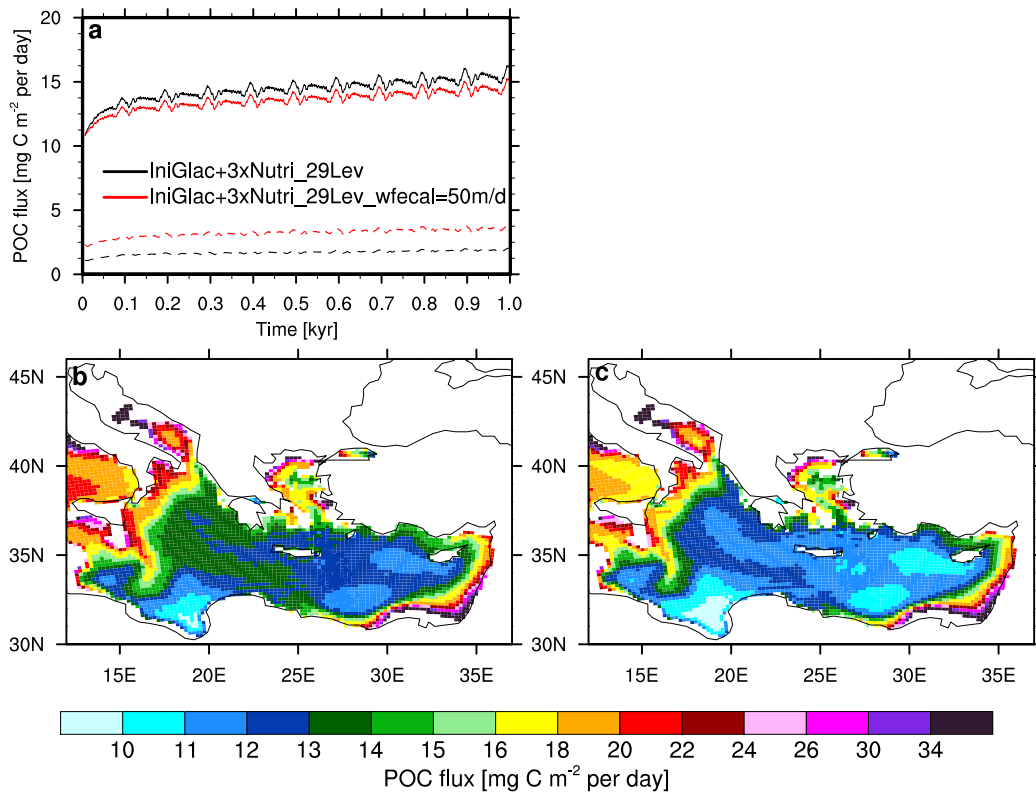
Supplementary Figure 9: Annual mean POC flux. Time series of POC flux smoothed with a 20-year running mean with solid lines showing the POC export production at the base of the euphotic zone (POC flux at 124 m depth) and dashed line showing the POC flux at 1,841 m depth (**a**). Maps of POC export production at 124 m depth for the IniGlac+3xNutri_29Lev experiment (**b**), and the IniGlac+3xNutri_29Lev_wefcal=50m/d experiment (**c**), each averaged between the simulation years 901 and 1,000. See Supplementary Note 4 for more details on these experiments.
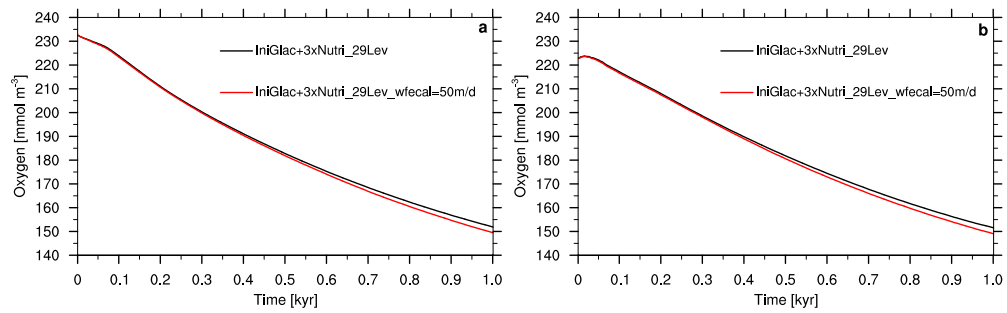
Supplementary Figure 10: Time evolution of the annual mean deep-water oxygen concentration. Oxygen concentration averaged over the Ionian Sea (**a**) and the Levantine Sea (**b**) at 2,416 m depth. Averaging areas as indicated by the respective boxes in Supplementary Figure 1. See Supplementary Note 4 for more details on these experiments.
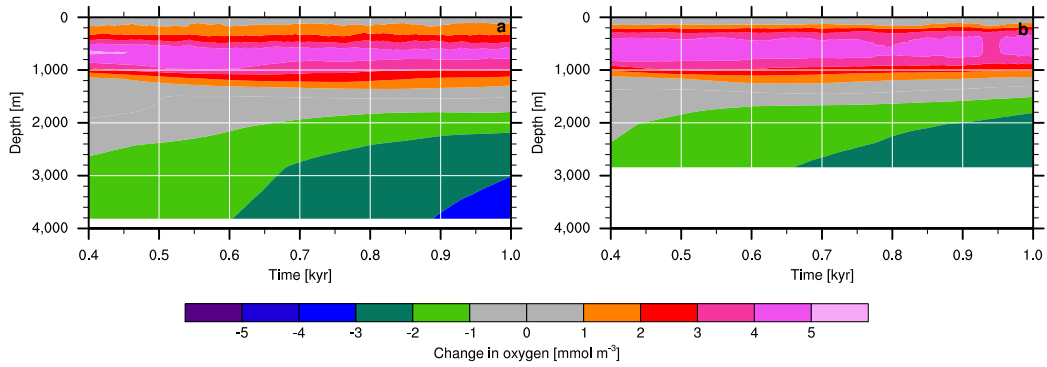
Supplementary Figure 11: Change in oxygen concentration. Hovmöller diagram of the change in oxygen concentration of the IniGlac+3xNutri_29Lev_wfecal=50m/d experiment relative to the IniGlac+3xNutri_29Lev experiment averaged over the Ionian Sea (**a**) and the Levantine Sea (**b**). Note that only the results between 0.4 and 1 kyr of simulation are illustrated. Averaging areas as indicated by the respective boxes in Supplementary Figure 1. See Supplementary Note 4 for more details on these experiments.
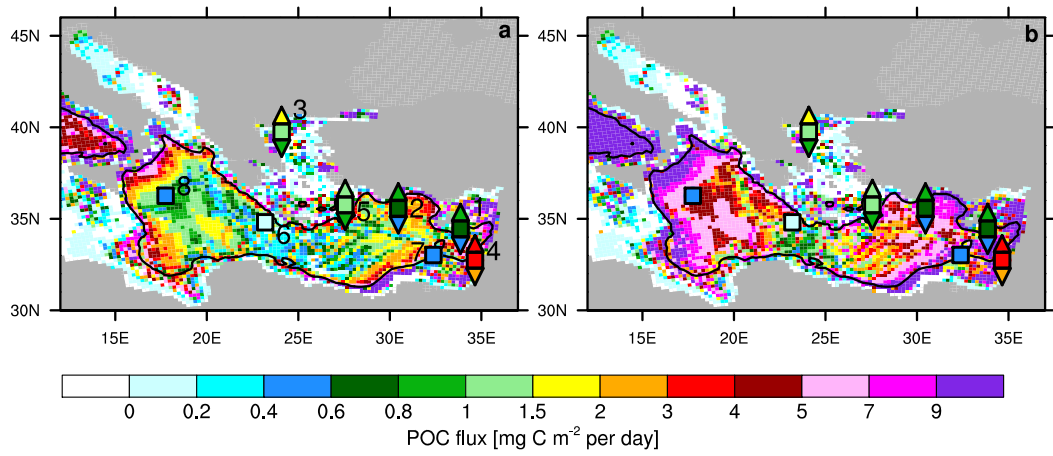
Supplementary Figure 12: Sediment POC burial flux. 100-year mean values averaged over the years 901-1,000 for the IniGlac+3xNutri_29Lev experiment (**a**) and the IniGlac+3xNutri_29Lev_wfecal=50m/d experiment (**b**). Model results are overlain with POC burial fluxes inferred from sediment cores, where mean fluxes (squares) and maximum/minimum values (upward/downward pointing triangles) represent the pre-sapropel period between 10.5 and 11.5 kyr ago, unless not otherwise given in the corresponding sediment core data source (see Supplementary Note 2 for more details). The black line marks the 1,500 m contour line. References of sediment cores given in Supplementary Figure 6. See Supplementary Note 4 for more details on these experiments.
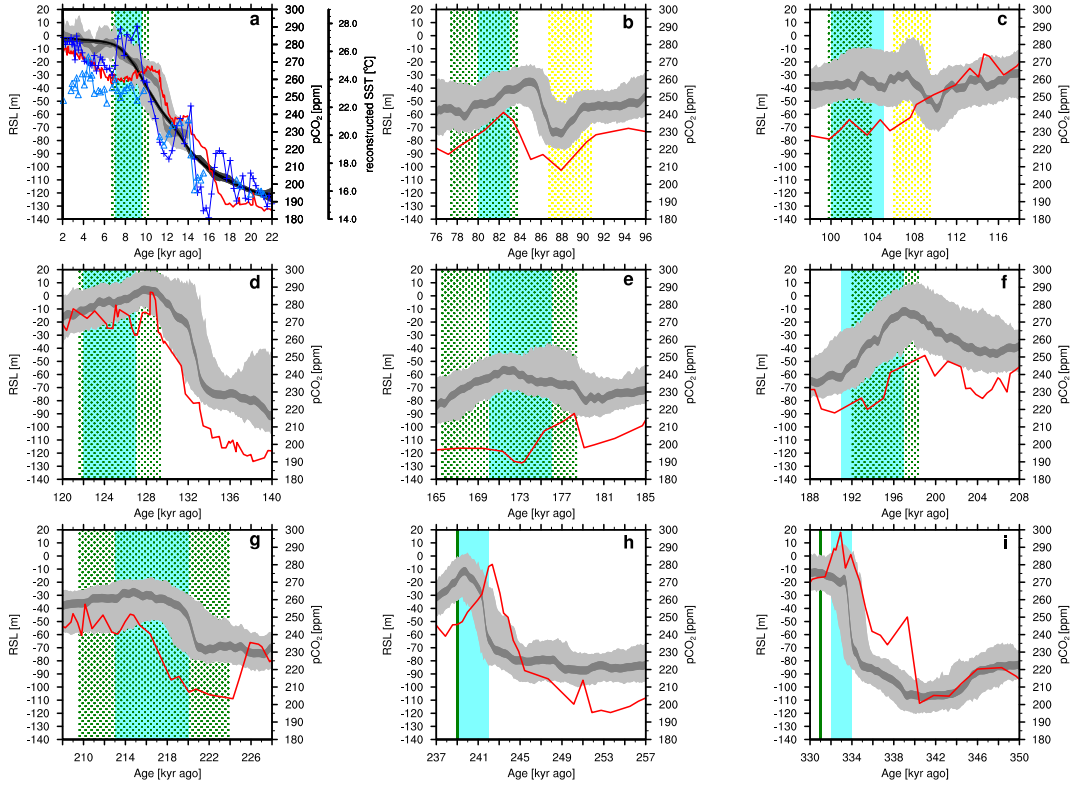
Supplementary Figure 13: Climatic proxy records for sapropel events S1 and S3 through S10. Sapropel events: S1 (**a**), S3 (**b**), S4 (**c**), S5 (**d**), S6 (**e**), S7 (**f**), S8 (**g**), S9 (**h**), S10 (**i**). Rectangles show sapropel ages (cyan[ref. 10]), (green dotted[ref. 11]) and precursory (yellow dotted (**b**,**c**)[ref. 11]). Green vertical lines show sapropel midpoint ages for S9 (**h**) and S10 (**i**)[ref. 11]. For the relative sea level (RSL) the 95 % probability interval (light grey) and the interval of the 95 % probability maximum of the RSL (dark grey) are shown[ref. 12]. For the last glacial-interglacial transition (**a**) RSL probabilities with 99 % confidence interval (light black) and 67 % confidence interval (black) are shown[ref. 13]. Red lines show composite atmospheric pCO_2 records[ref. 14]. For the last glacial-interglacial transition (**a**) sea surface temperature (SST) reconstructions based on $U^{k'}_{37}$ (light blue triangles) and TEX_{86} (dark blue crosses) records from the eastern Levantine Sea are shown[ref. 15]. See Supplementary Note 5 for more details.

Supplementary Tables

Supplementary Table 1: Prescribed river input rates. River run-off [m^3 s^{-1}], dissolved phosphate and dissolved nitrate [mol s^{-1}] input rates. EMSRIV: River input rates of all rivers draining into the EMS. NILERIV: Nile river input rates.

Experiment	EMSRVI	NILERIV	EMSRVI	NILERIV	EMSRVI	NILERIV
	river run-off		total dissolved phosphate		dissolved nitrate	
Baseline	9518	5358	33.3	16.9	510.1	141.5
3xNutri	9518	5358	99.8	50.7	1530.3	424.5
Nile	18518	14358	61.7	45.2	747.7	379
IniGlac	9518	5358	33.3	16.9	510.1	141.5
IniGlac+3xNutri	9518	5358	99.8	50.7	1530.3	424.5

Supplementary Table 2: Initial conditions of physical and biogeochemical tracers. Subbasins: Atlantic Ocean (ATL), EMS, Western Mediterranean Sea (WMS), Mediterranean Sea (MS).

Tracer	Initial value	Region	Unit
Salinity	38	MS, ATL	psu
Temperature	20	MS, ATL	$^{\circ}$C
Dissolved phosphate	0.35	ATL, WMS	$mmol\,P\,m^{-3}$
Dissolved phosphate	0.2	EMS	$mmol\,P\,m^{-3}$
Dissolved nitrate	7	MS, ATL	$mmol\,N\,m^{-3}$
Dissolved oxygen	185	MS, ATL	$mmol\,O\,m^{-3}$
Dissolved silica	8	MS, ATL	$mmol\,Si\,m^{-3}$
Dissolved inorganic carbon	2270	MS, ATL	$mmol\,C\,m^{-3}$
Alkalinity	2370	MS, ATL	$mmol\,eq\,m^{-3}$
Dissolved organic carbon	10^{-4}	MS, ATL	$mmol\,C\,m^{-3}$
Refractory dissolved organic carbon	$8.2 \cdot 10^{-7}$	MS, ATL	$mmol\,P\,m^{-3}$
Iron	$0.6 \cdot 10^{-3}$	MS, ATL	$mmol\,Fe\,m^{-3}$
Phytoplankton	$1 \cdot 10^{-5}$	MS, ATL	$mmol\,P\,m^{-3}$
Zooplankton	$1 \cdot 10^{-5}$	MS, ATL	$mmol\,P\,m^{-3}$
POC (dead phyto- and zooplankton)	$1 \cdot 10^{-8}$	MS, ATL	$mmol\,P\,m^{-3}$
POC (zooplankton fecal pellets)	$1 \cdot 10^{-8}$	MS, ATL	$mmol\,P\,m^{-3}$
Calcium carbonate	$1 \cdot 10^{-2}$	MS, ATL	$mmol\,C\,m^{-3}$
Opal-shells	$1 \cdot 10^{-2}$	MS, ATL	$mmol\,Si\,m^{-3}$
Dust	1	MS, ATL	$mg\,m^{-3}$
Sediment POC	$122 \cdot 10^{3}$	MS, ATL	$mmol\,C\,m^{-3}$
Sediment calcium carbonate	$1 \cdot 10^{-2}$	MS, ATL	$mmol\,C\,m^{-3}$
Sediment opal-shells	$1 \cdot 10^{-2}$	MS, ATL	$mmol\,Si\,m^{-3}$
Sediment clay	0	MS, ATL	$mg\,m^{-3}$
Sediment sand	$2570 \cdot 10^{6}$	MS, ATL	$mg\,m^{-3}$

Supplementary Note 1: The circulation of the EMS

The main near-surface circulation features of all model experiments are similar to patterns observed today[16]. Intermediate water forms today in the cyclonic Rhodes gyre in the northern Levantine Sea[16–18] (subregions of the EMS are shown in Supplementary Figure 1). In all early Holocene experiments, intermediate water formation is shifted into the northern Aegean Sea as indicated by the mixed-layer pattern of intermediate depths (Supplementary Fig. 3). This is because the missing, relatively fresh Black Sea inflow (the connection between the Black Sea and the Mediterranean Sea is closed in our experimental setup, (see main text, Methods)) leads to an accumulation of highly saline water in the northern Aegean Sea. This dense, saline water flows along the Greek coast towards the Adriatic Sea, where it entrains less dense waters of the northern Ionian Sea, and thus appears as a mixed-layer pattern in Supplementary Figure 3. In the Adriatic Sea, the model simulates the formation of dense Adriatic deep water during winter. This newly formed water flows along the western boundary into the Ionian Sea and, if it is dense enough, forms eastern Mediterranean deep water (EMDW).

Supplementary Figure 4 illustrates the transport profile at 38.8°N between Italy and Greece as computed from the annual mean meridional overturning stream function, integrated across the Adriatic and northern Ionian Sea. Over the course of the simulations, the Baseline experiment shows high transport rates down to the sea floor with the frequency of these events following the occurrence of cold winters in the 100-year repeating atmospheric forcing cycle. Both the Nile and IniGlac experiment show an initial strong reduction and subsequent gradually increasing depth penetration of the dense water formed in the Adriatic Sea. The penetration depth of the dense water formed in the Adriatic Sea is controlled by the strength of the density stratification in the northern Ionian Sea, which is more strongly developed in the IniGlac than in the Nile experiment. Therefore, dense-water transport is simulated at greater depth in the Nile than in the IniGlac simulation.

Supplementary Note 2: Sediment POC burial

In the main text, we show maps comparing POC burial flux observations with simulated POC burial fluxes for the pre-sapropel and sapropel period (main text Fig. 4). For a more detailed comparison, Supplementary Figure 6 displays a scatter plot of the simulated POC sediment burial fluxes vs. the observed burial fluxes. As outlined in the main text, for the pre-sapropel

period, the Baseline experiment is in reasonable agreement with observations. In contrast, the Nile, 3xNutri, and IniGlac+3xNutri (pre-sapropel) experiments deviate from reconstructed fluxes in their mean fluxes, particularly above 2000 m. The IniGlac experiment agrees best with observations of the pre-sapropel period. Deep-water anoxia is only simulated in the IniGlac+3xNutri experiment, hence only this experiment can be compared with observational records of the S1 period. More details on regional patterns of the POC burial flux are given in Grimm[18].

For the sediment core observations, the conversion from concentrations to fluxes requires knowledge of the sedimentation rates and dry bulk density, which is not yet widely available for cores covering the pre-sapropel period. This explains why we have only few samples for comparison of the pre-sapropel period. For the sapropel period, we have a rather good spatial coverage of sediment POC burial fluxes.

For the sediment cores, for which the POC burial flux was not provided by the authors of the dataset, and no dry bulk density was available, we used for the pre-sapropel interval a mean dry bulk density of $1 \, \mathrm{g \, cm^{-3}}$ (Supplementary Fig. 6a-e, core labels 1, 2, 6, 7), and for the sapropel interval $0.7 \, \mathrm{g \, cm^{-3}}$ (Supplementary Fig. 6f, core labels 4, 5, 8, 9, 10, 11, 15). These dry bulk density values were derived from the mean dry bulk densities of the other cores for the corresponding time-slice intervals. For those cores, for which no age model exists, we used for the sapropel period the depth interval as given in the corresponding sediment cores references in Supplementary Figure 6f (core labels 8, 9, 10, 11, 14). For the pre-sapropel period (Supplementary Fig. 6a-e) we used the depth levels a few cm below the sapropel; for core label 6: 22-23 cm, and for core label 8: 84 cm.

Supplementary Note 3: Sensitivity of the IniGlac deep-water stagnation to cold events

The last glacial-interglacial transition since the Heinrich event 1 (H1, 18-15.5 ka)[19] is characterized by short-term climate fluctuations such as the Bølling-Allerød[20], the Younger Dryas (12.8 to 11.6 kyr ago)[21] or a cold event centred around 8.2 kyr ago[22]. While the climate of the northern borderlands of the EMS during the Bølling-Allerød was similar to the climate during the early Holocene, the Younger Dryas was characterized by an abrupt change to cold and dry conditions[20]. The cold event centred around 8.2 kyr ago has been shown to have interrupted S1 deposition[22, 23]. Modelling results show that the

S1 interruption around 8.2 kyr ago resulted from enhanced deep-water formation in the Adriatic Sea, and its subsequent spreading into the main EMS basin[24]. This is also confirmed by our compilation of foraminiferal δ^{13}C proxy records, which shows partial renewal of deep water for the 8.2 kyr cold event. In addition, our foraminiferal δ^{13}C proxy records suggest partial renewal of deep-water during the Younger Dryas (see main text Fig. 5). During the Younger Dryas the average annual temperature in the Aegean region was 6°C cooler than in the preceding Bølling-Allerød intervall[20], with the mean temperature anomaly of the coldest month ranging as low as -8°C to -10°C[ref. 25]. In addition, the annual precipitation in the Aegean region decreased by 300 mm[ref. 20], reflecting more arid conditions during the Younger Dryas compared to the Bølling-Alllerød. The temperature change in the Adriatic Sea, in the central Mediterranean region around Italy, and in western Greece was not as strong as in the Aegean region for the time of the Younger Dryas (see citations in Kotthoff et al.[20]).

Here, we assess the sensitivity of the IniGlac experiment towards changes in the surface buoyance loss, and quantify the imprint of the Younger Dryas on the IniGlac experiment. We choose to start these sensitivity experiments after 3.5 kyr of simulation of the IniGlac experiment because this point in time reflects the onset of the Younger Dryas, given that the stagnation was initiated at $\sim$16 kyr ago. In the Adriatic Sea, the Aegean Sea, and the Gulf of Lions we impose an additional 2°C cooling (IniGlac_-2 experiment) and 6°C cooling (IniGlac_-6 experiment) on the 2 m air temperature and dew point temperature of the 100-year daily atmospheric forcing fields (see main text Methods), and force the model with this "new" forcing in a loop. In order to reduce the computational burden, the biogeochemistry was not included in these experiments. As in the IniGlac experiment, the inflow of the Atlantic hydrographic properties resembles the early Holocene conditions. The IniGlac_-2 experiment was run for 600 years, and the IniGlac_-6 was run for 800 years. Only the IniGlac_-6 experiment is within the range of climatic changes that can be expected for the Younger Dryas, while the IniGlac_-2 experiment might be too warm.

Based on the analyses of oxygen concentration in the Ionian Sea in the IniGlac experiment (see main text Fig. 2), we use the apparent water age deviation (A_D) (see main text Methods) A_D=80 % averaged over the Ionian Sea as the depth of the WPI, which marks the interface depth between the well-ventilated upper ocean and the partially-ventilated intermediate water masses. As in our main experiments, we use A_D=30 % for the depth of the VSI, below which changes in water properties are limited to cross-isopycnal diffusion. The depth range between A_D 30 % and 80 % shows the layer of partial reventilation. Within the partially ventilated ocean layer water

properties such as A_M or the oxygen content are a mixture of older previous stagnant and freshly formed deep or intermediate water mass properties.

In both sensitivity experiments, enhanced mixing and formation of dense water is simulated in the Adriatic Sea and the Aegean Sea. As in the IniGlac experiment, by far the largest part of the dense water spreading into the EMS is formed in the Adriatic Sea (Supplementary Fig. 3), and from there spreads into the Ionian and subsequently into the Levantine Sea (main text Fig. 1, Supplementary Fig. 2). Thus, the changes in the Ionian Sea are more strongly developed than in the Levantine Sea, hence we focus our analysis on the Ionian Sea.

In both experiments, the additional cooling applied in the northern regions reduces the net evaporation, which results in a basin-wide freshening of the surface ocean in the EMS (Supplementary Fig. 7). A general cooling applied over the entire EMS would further reduce the net evaporation in the EMS compared to the sensitivity experiments, and thus would more strongly decrease the surface salinity in the whole basin. This then would counteract the effect of lower temperatures on density, and thus would lead to a reduced density increase of newly formed water in the Adriatic Sea. However, the climate of the Younger Dryas was more arid than the preceding Bølling-Allerød, which possibly increased the surface ocean salinity, and thus to some extent compensated for the enhanced freshening due to the reduced evaporation as simulated in our sensitivity experiments.

In the IniGlac_-2 experiment, the extended period of mixing and dense-water formation and its subsequent spreading into the EMS is reflected by the decreasing A_M between ∼700 and 1,400 m relative to the IniGlac experiment (Supplementary Fig. 8a). Compared to the IniGlac experiment, the position of both the WPI and the VSI is unchanged, indicating that the deep EMS is not affected by this moderate cooling in the IniGlac_-2 experiment. A similar finding, with partial water renewal down to ∼1,250 m depth was reported in a previous modelling study, in which a 2°C and 3°C cooling was applied to the Adriatic Sea, the Aegean Sea and the Gulf of Lions for the time of S1 deposition[24].

In contrast, in the IniGlac_-6 experiment, more intense mixing and denser water formation results in stronger changes in the A_M at intermediate depth compared to the changes simulated in the IniGlac_-2 experiment (Supplementary Fig. 8b). In addition, the spreading of denser water at greater depth levels pushes the older water upward, which is illustrated by the initial positive change in A_M above ∼700 m depth (Supplementary Fig. 8b). It can also be expected that more nutrients would be pushed upward, and possibly fuel higher biological production, as was reconstructed for the Younger Dryas compared to the Bølling-Allerød and the early Holocene[26]. Higher produc-

tion in turn would lead to higher oxygen utilisation at depth, which possibly to some extent compensates for the enhanced physical ventilation. In the IniGlac_-6 experiment, the depth of the WPI first deepens and after ∼200 years slowly levels out at 1,200 m depth, which is around 200 m deeper than in the IniGlac experiment (Supplementary Fig. 8b). Over time, the deep vertical density gradient in the IniGlac_-6 experiment is eroded faster than in the IniGlac experiment, and thus the partially ventilated ocean layer penetrates faster into greater depths, which is illustrated by the slightly faster deepening of the VSI depth in the IniGlac_-6 experiment than in the IniGlac experiment. Although intermediate partial reventilation is enhanced in the IniGlac_-6 experiment, the deep ocean below the VSI is almost unaffected by these changes. Overall, the results indicate that the IniGlac_-6 experiment shows no potential to fully reventilate the deep EMS within the ∼1.2 kyr of Younger Dryas duration.

In summary, we show that the cooling during the Younger Dryas increases the partial ventilation at mid depth, while the deep stagnating EMS is almost unaffected by these climatic conditions, and continuous deep-water oxygen utilisation persists (IniGlac_-6 experiment). This demonstrates that the Younger Dryas cold event did not fully interrupt the stagnation period triggered near the end of H1, as simulated in the IniGlac experiment. With the termination of the Younger Dryas, enhanced warming and freshening (see main text) would then quickly reinforce deep-water stagnation in the EMS.

Supplementary Note 4: Sensitivity to the sinking speed of POC

It was suggested that in areas of rapid POC posting to depth, anoxia only developed in "blankets" draped over the sea-floor, at least in depths shallower than 2000 m[ref. 27]. 1-dimensional ecosystem model simulations showed that an increase of the POC sinking velocity leads to a combined development of anoxia below the ventilation-stagnation interface (VSI) and the bottom water[28]. This finding, with formation of an anoxic bottom-water layer, while parts of the deep-water column still contain oxygen, might explain the occurrence of anoxic "blankets". Under the static ocean circulation in the 1-dimensional model[28], frequent reventilation of the anoxic blankets are not simulated, yet this is a major characteristic in the description of the sediment records that were used in the formulation of the anoxic blanket theory[27]. Besides, to justify the EMS basin-wide occurrence of larger-sized POC that sinks faster to the sea floor, changes in the pelagic ecosystem and/or the

development of a deep chlorophyll maximum are required. Such conditions, however, have only been reconstructed for the last glacial maximum and earlier sapropels (S3, S4, S5, S7), and only in the very eastern Mediterranean also for S1[ref. 29–31]. Nevertheless, we here show a sensitivity experiment similar to the ones presented by Bianchi et al.[28] to see whether we can simulate an anoxic layer at the sea floor and/or significantly reduce the time required to develop full deep-water anoxia.

In our default model setup, the POC pool is divided into a slow sinking dead phyto- and zooplankton pool, and a fast sinking zooplankton fecal pellets pool, and individual sinking velocities are assigned to both of these POC classes (wplankton=1.5 m per day, wfecal=25 m per day) (see main text Methods). We have tuned the default sinking velocities to fit the present day EMS phosphate profile, the POC flux measured in the sediment traps, and the POC burial flux[18]. In our sensitivity experiment, we doubled the sinking speed of the fast sinking POC pool (wfecal=50 m per day), and kept the slow sinking POC components (wplankton=1.5 m per day) unchanged. We ran this configuration within the IniGlac+3xNutri experiment using a coarse vertical resolution setup (29 layers instead of the presented 46 layers in all other experiments, see main text Methods). The default experiment is called the IniGlac+3xNutri_29Lev, and the sensitivity experiment with enhanced sinking velocity IniGlac+3xNutri_29Lev_wfecal=50m/d. The differences due to the coarser vertical resolution setup (IniGlac+3xNutri vs. IniGlac+3xNutri_29Lev) are detailed in Grimm[18].

The sensitivity experiment shows that a doubling of the fecal pellets sinking velocity reduces the POC export out of the euphotic zone, and in turn enhances the POC flux at depth (Supplementary Fig. 9). The faster downward transport of POC leads to an increased vertical nutrient gradient, and thus less nutrients are available for biological production because nutrients are trapped in the deep stagnating ocean. Notable changes in the deep-water oxygen content are only observed after ∼400 years of simulation (Supplementary Fig. 10). Overall, the vertical change in POC flux leads to higher oxygen concentrations in the upper ∼1,200 m, and to an increased oxygen utilization at depth (Supplementary Fig. 11). The total change of the oxygen consumption is only small, yielding after 1 kyr of simulation around 3 to 4 mmol m^{-3} more oxygen depletion below ∼2,000 m for a doubling of wfecal. This is only a minor effect compared to the total oxygen reduction within this period of 70 to 80 mmol m^{-3} (Supplementary Fig. 10). By far, the largest part of the enhanced POC flux at depth is accumulated in the sediment (Supplementary Fig. 12). In the sediment, the additional oxygen utilization is stronger than in the water column, and amounts to ∼8 mmol m^{-3} after 1 kyr of simulation, however, no pore-water anoxia is simulated.

21

In summary, enhancing the sinking velocity of the fecal pellets component of the POC pool does not lead to the development of a bottom-water nor sediment pore-water anoxia after 1 kyr of simulation. Based on the rather small change of the oxygen content in the deep EMS and in the sediment, anoxic conditions at the sea floor would not evolve much before full deep-water anoxia develops. Thus, there is no significant reduction in the time required to develop deep-water anoxia when enhancing the POC sinking velocity. This sensitivity experiment further reinforces our findings that the formation of frequently reventilated anoxic "blankets" trapped over the sea floor is restricted to the vicinity where the change from oxic to dysoxic to anoxic conditions is simulated (the depth of the VSI). Thus, the regional and vertical extent at which anoxic "blankets" are found in sediment core records marks the depth range of the vertical oscillation of the VSI (see main text).

Supplementary Note 5: Applicability of our results for S1 formation to older sapropel events

In the main text, we conclude that the timing and strength of warming and freshening (freshening in the Mediterranean Sea due to rising sea level and corresponding enhanced exchange through the Strait of Gibraltar, but also freshening of the inflowing Atlantic water, and enhanced other moisture sources e.g. insolation-driven strength of African run-off) is crucial for the onset and the strength of the S1 deep-water stagnation. At the termination of H1, enhanced SST warming was reconstructed throughout the EMS[15,32,33], and coincides with the first rapid rise in atmospheric pCO$_2$ at ∼16 kyr ago (Supplementary Fig. 13a). Sea-level rise started to accelerate at ∼17 kyr ago, and was significantly enhanced during Meltwater peak 1A and Meltwater peak 1B[13,34,35] (Supplementary Fig. 13a). Insolation-driven intensified Nile run-off emerged after 14 kyr ago and was strongly enhanced after 12 kyr ago[21]. Both our modelling results and proxy data show that the onset of the deep-water stagnation was during or near the end of H1 (see main text). Therefore, it appears that the rapid late glacial surface warming of the EMS preconditioned the S1 deep-water stagnation, and over time, the deep-water stagnation was restrengthened by the rising sea level, in particular during the phases of Meltwater peak 1A and 1B, and the intensification of other latest Pleistocene to early Holocene moisture sources (see main text).

During the late Quaternary ten sapropel layers were identified in the EMS[10,11]. Of those, three other sapropels (in addition to S1) occurred subsequently or towards the end of major glacial terminations (S5 at Termination

II, S9 at Termination III, S10 at Termination IV). Here we use global records of sea level and atmospheric CO_2 concentration as proxies for the local climatic conditions in the EMS (Supplementary Fig. 13). From these records we infer the relative timing of the first strong increase in atmospheric CO_2 concentrations (as a proxy for surface warming), the phases of strong sea-level rise (as indicators for surface freshening) and the onset of S5, S9 and S10. This yields an estimate of the potential role of these climatic changes for the formation of these sapropels. For S9 and S10 Ziegler et al.[11] give only the midpoint age, from which we derive estimates of the age of the beginning of S9 and S10 by combining each midpoint age with the corresponding duration of these sapropels given in Emeis et al.[10].

During Termination II, the first period with a rapid rise in both atmospheric CO_2 concentration and sea level starts approximately at $\sim$133.5 kyr ago, which is $\sim$6.5 kyr or $\sim$4 kyr prior to the onset of S5 deposition. The time frames are inferred by the RSL probability maximum, atmospheric CO_2 concentration and the onset ages of S5 (Supplementary Fig. 13d). Even though there are large uncertainties in the dating of the S5 event, the amplitude and timing of the rapid rise in pCO_2 and sea level are rather similar to S1. However, in contrast to S1, the onset of the rapid pCO_2 and sea-level rise occur in parallel, and therefore the stagnation of the circulation leading to S5 deep-water anoxia was possibly even stronger than the stagnation during S1 formation.

During Termination III, the first rapid rise in atmospheric CO_2 concentration occurs at $\sim$245.5 kyr ago, and thus precedes the onset of S9 deposition by $\sim$3.5 kyr or possibly $\sim$5 kyr (Supplementary Fig. 13h). The rate of change between the onset of the first rapid rise in atmospheric CO_2 concentration and the onset of sapropel deposition was larger during Termination III than during Termination I, which further suggests that the strength of the deep-water stagnation due to the warming prior to S9 deposition was stronger than during S1. The first rapid sea-level rise occurred $\sim$3 kyr after the first rapid rise in pCO_2, so $\sim$0.5 kyr or possibly $\sim$2 kyr prior to S9 deposition. A gradual increase in sea-level can be seen already $\sim$1 kyr after the first rapid rise in pCO_2. This gradual sea-level rise possibly provided the necessary EMS upper-ocean density reduction to restrengthen the stagnation initiated by the inferred rapid warming signal.

During Termination IV, we infer the first rapid rise of atmospheric CO_2 concentration at $\sim$340.5 kyr ago, which is $\sim$6.5 or possibly $\sim$8.5 kyr prior to the onset of S10 deposition (Supplementary Fig. 13i). The first rapid rise in sea level precedes S10 deposition by 0.5 or possibly $\sim$2.5 kyr. Even though the onset of the first rapid sea-level rise in relation to the onset of the first rapid rise in atmospheric CO_2 concentration is rather late, the contin-

23

uous rising sea level in parallel to the rising pCO_2 might have continuously provided the necessary upper-ocean density reduction to develop the EMS deep-water stagnation before the first rapid sea-level rise started.

Although the other late Quaternary sapropels (S3, S4, S6, S7 and S8) formed with no major glacial termination preceding their onsets, the relatively low sea level during their formation (Supplementary Fig. 13b,c,e,f,g) must have supported the accumulation of nutrients in the EMS due to the reduced exchange at the Strait of Gibraltar. This would have fuelled higher production, as has been proposed for the formation of S6[ref. 36], and resulted in high oxygen consumption in the deep layers. Under such eutrophic conditions, the time to reach anoxia in stagnant deep water would be short, and even a comparatively small perturbation (such as enhanced Nile river run-off) should be sufficient for sapropel formation, as has been suggested for S8 formation[10]. This could explain the close link between Quaternary sapropel events and insolation-driven intensification of African river run-off draining into the EMS[37,38].

In summary, even though the uncertainties in all records shown are large, we find that the timing and the strength of the first rapid pCO_2 rise (warming) and sea-level rise (freshening) prior to the deposition of S5, S9 and S10 are rather similar to the conditions prior to S1 deposition. Therefore, we hypothesise that our mechanistic explanation of S1 formation hinging on density contrasts between old deep water emplaced near the end of the glacials and an increasingly buoyant surface layer during the deglaciation also holds for at least S5, S9 and S10. To confirm this hypothesis more research on these older sapropel events is necessary.

Supplementary References

[1] Schmidt, A. Reconstruction of the late Quaternary deep-sea ecosystem in the eastern Levantine Basin using benthic foraminifera and stable isotopes *Diploma thesis, University of Leipzig* (2007).

[2] Milker, Y., Ehrmann, W. & Schmiedl, G. Spätquartäre Sedimentationsgeschichte im östlichen Mittelmeer. *Diploma thesis, University of Leipzig, Germany* (2006).

[3] Kuhnt, T. Reconstruction of late Quaternary deep-sea ecosystem variability in the eastern Mediterranean Sea based on benthic foraminiferal faunas and stable isotopes. *Doctoral thesis, University of Leipzig, Germany* (2008).

[4] Möbius, J. *et al.* Geochemistry on Holocene sediments from the Mediterranean. doi:10.1594/PANGAEA.758621 (2011). Supplement to: Möbius, J. Lahajnar, N. & Emeis, K.-C. Diagenetic control of nitrogen isotope ratios in Holocene sapropels and recent sediments from the Eastern Mediterranean Sea. *Biogeosciences* **7,** 3901-3914 (2010).

[5] Möbius, J. Isotope fractionation during organic nitrogen remineralization (ammonification): Implications for nitrogen isotope biogeochemistry. *Geochim. Cosmochim. Acta* **105,** 422-432 (2013).

[6] Fontugne, M.R. & Calvert, S.E. Table 1a. Compositional data on core MD84-641. doi:10.1594/PANGAEA.55449 (1992). In Supplement to: Fontugne, M. R. & Calvert, S. E. Late Pleistocene Variability of the Carbon Isotopic Composition of Organic Matter in the Eastern Mediterranean: Monitor of Changes in Carbon Sources and Atmospheric CO_2 Concentrations. *Paleoceanography* **7,** 1-20 (1992).

[7] Gallego-Torres, D. *et al.* Sedimentology and geochemical analyses of Pliocene to Holocene sediments of ODP Hole 160-964A in the eastern Mediterranean Sea (Appendix). doi:10.1594/PANGAEA.693913 (2007). Supplement to: Gallego-Torres, D., Martinez-Ruiz, F. C., Paytan, A., Jiménez-Espejo, F. J. & Ortega-Huertas, M. Pliocene-Holocene evolution of depositional conditions in the eastern Mediterranean: Role of anoxia vs. productivity at time of sapropel deposition. *Palaeogeogr. Palaeoclimatol. Palaeoecol.* **246,** 424-439 (2007).

[8] Slomp, C. P., Thomson, J. & de Lange, G. J. Enhanced regeneration of phosphorus during formation of the most recent eastern Mediterranean sapropel (S1). *Geochim. Cosmochim. Acta* **66,** 1171-1184 (2002).

[9] Slomp, C. P., Thomson, J. & de Lange, G. J. Controls on phosphorus regeneration and burial during formation of eastern Mediterranean sapropels. *Mar. Geol.* **203,** 141-159 (2004).

[10] Emeis, K.-C. *et al.* Eastern Mediterranean surface water temperatures and $\delta^{18}O$ composition during deposition of sapropels in the late Quaternary. *Paleoceanography* **18,** doi: 10.1029/2000PA000617 (2003).

[11] Ziegler, M., Tuenter, E. & Lourens, L. J. The precession phase of the boreal summer monsoon as viewed from the eastern Mediterranean (ODP Site 968). *Quat. Sci. Rev.* **29,** 1481-1490 (2010).

[12] Grant, K. M. *et al.* Sea-level variability over five glacial cycles. *Nat. Commun.* **5,** doi:10.1038/ncomms6076 (2014).

[13] Stanford, J. D. *et al.* Sea-level probability for the last deglaciation: A statistical analysis of far-field records. *Glob. Planet. Chang.* **79,** 193-203 (2011).

[14] Lüthi, D. *et al.* High-resolution carbon dioxide concentration record 650,000-800,000 years before present. *Nature* **453,** 379-382 (2008).

[15] Castañeda, I.S. *et al.* Radiocarbon dating and alkenone-based proxies of sediment core GeoB7702-3. doi:10.1594/PANGAEA.736918 (2010). Supplement to: Castañeda, I. S. *et al.* Millennial-scale sea surface temperature changes in the eastern Mediterranean (Nile River Delta region) over the last 27,000 years. *Paleoceanography* **25,** doi:10.1029/2009PA001740 (2010).

[16] Pinardi, N. & Masetti, G. Variability of the large scale general circulation of the Mediterranean Sea from observations and modelling: a review. *Palaeogeogr. Palaeoclimatol. Palaeoecol.* **158,** 153-173 (2000).

[17] Adloff, F. *et al.* Upper ocean climate of the Eastern Mediterranean Sea during the Holocene Insolation Maximum - a model study. *Clim. Past* **7,** 1103-1122, (2011).

[18] Grimm, R. *Simulating the early Holocene eastern Mediterranean sapropel formation using an ocean biogeochemical model.* Rep. Earth Syst. Sci. **123,** Max Planck Institute for Meteorology Available at: http://www.mpimet.mpg.de (2012).

[19] Bard, E., Rostek, F., Turon, J.-L. & Gendreau, S. Hydrological Impact of Heinrich Events in the Subtropical Northeast Atlantic. *Science* **289,** 1321-1324 (2000).

[20] Kotthoff, U. *et al.* Impact of Lateglacial cold events on the northern Aegean region reconstructed from marine and terrestrial proxy data. *J. Quat. Sci.* **26,** 89-96 (2011).

[21] Revel, M. *et al.* 100,000 Years of African monsoon variability recorded in sediments of the Nile margin. *Quat. Sci. Rev.* **29,** 1342-1362 (2010).

[22] Rohling, E. J., Jorissen, F. J. & De Stigter, H. C. 200 Year interruption of Holocene sapropel formation in the Adriatic Sea. *J. Micropalaeontol.* **16,** 97-108 (1997).

[23] Schmiedl, G. *et al.* Climatic forcing of eastern Mediterranean deep-water formation and benthic ecosystems during the past 22 000 years. *Quat. Sci. Rev.* **29,** 3006-3020 (2010).

[24] Myers, P. G. & Rohling, E. J. Modeling a 200-Yr Interruption of the Holocene Sapropel S_1. *Quat. Res.* **53,** 98-104 (2000).

[25] Dormoy, I. *et al.* Terrestrial climate variability and seasonality changes in the Mediterranean region between 15 000 and 4000 years BP deduced from marine pollen records. *Clim. Past* **5,** 615-632 (2009).

[26] Abu-Zied, R. H. *et al.* Benthic foraminiferal response to changes in bottom-water oxygenation and organic carbon flux in the eastern Mediterranean during LGM to Recent times. *Mar. Micropaleontol.* **67,** 46-68 (2008).

[27] Casford, J. S. L. *et al.* A dynamic concept for eastern Mediterranean circulation and oxygenation during sapropel formation. *Palaeogeogr. Palaeoclimatol. Palaeoecol.* **190,** 103-119 (2003).

[28] Bianchi, D. *et al.* Simulations of ecosystem response during the sapropel S1 deposition event. *Palaeogeogr. Palaeoclimatol. Palaeoecol.* **235,** 265-287 (2006).

[29] Rohling, E. J. & Gieskes, W. W. C. Late Quaternary changes in Mediterranean intermediate water density and formation rate. *Paleoceanography* **4,** 531-545 (1989).

[30] Castradori, D. Calcareous nannofossils and the origin of eastern Mediterranean sapropels. *Paleoceanography* **8,** 459-471 (1993).

[31] Kemp, A. E. S., Pearce, R. B., Koizumi, I., Pike, J. & Rance, S. J. The role of mat-forming diatoms in the formation of Mediterranean sapropels. *Nature* **398,** 57-61 (1999).

[32] Essallami, L., Sicre, M. A., Kallel, N., Labeyrie, L. & Sian, G. Hydrological changes in the Mediterranean Sea over the last 30,000 years. *Geochem. Geophys. Geosyst.* **8,** Q07002, doi:10.1029/2007GC001587 (2007).

[33] Sicre, M.-A., Siani, G., Genty, D., Kallel, N. & Essallami, L. Seemingly divergent sea surface temperature proxy records in the central Mediterranean during the last deglaciation. *Clim. Past* **9,** 1375-1383 (2013).

[34] Fairbanks, R. G. A 17,000-year glacio-eustatic sea level record: influence of glacial melting rates on the Younger Dryas event and deep-ocean circulation. *Nature* **342,** 637-642 (1989).

[35] Bard, E., Hamelin, B. & Fairbanks, R. G. U-Th ages obtained by mass spectrometry in corals from Barbados: sea level during the past 130,000 years. *Nature* **346,** 456-458 (1990).

[36] Schmiedl, G., Hemleben, C., Keller, J. & Segl, M. Impact of climatic changes on the benthic foraminiferal fauna in the Ionian Sea during the last 330,0000 years. *Paleoceanography* **13,** 447-458 (1998).

[37] Rossignol-Strick, M., Nesteroff, W., Olive, P. & Vergnaud-Grazzini, C. After the deluge: Mediterranean stagnation and sapropel formation. *Nature* **295,** 105-110 (1982).

[38] Rossignol-Strick, M. Mediterranean Quaternary sapropels, an immediate response of the African monsoon to variation of insolation. *Palaeogeogr. Palaeoclimatol. Palaeoecol.* **49,** 237-263 (1985).